One-dimensional multiferroic semiconductor WOI_3: Unconventional anisotropic d^1 rule and bulk photovoltaic effect

Zhihao Gong [1,*] Yechen Xun,[2,*] Zhuang Qian,[3] Kai Chang,[4] Jingshan Qi,[5,†] and Hua Wang [4,‡]

[1]*Academy of Interdisciplinary Studies on Intelligent Molecules, Tianjin Key Laboratory of Structure and Performance for Functional Molecules, College of Chemistry, Tianjin Normal University, Tianjin 300387, China*

[2]*Department of Physics and Astronomy, The University of Tennessee, Knoxville, Tennessee 37996, USA*

[3]*Institute of Natural Sciences, Westlake Institute for Advanced Study, Hangzhou, Zhejiang 810024, China*

[4]*Center for Quantum Matter, School of Physics, Zhejiang University, Hangzhou 310058, China*

[5]*Tianjin Key Laboratory of Quantum Optics and Intelligent Photonics, School of Science, Tianjin University of Technology, Tianjin 300384, China*

(Received 13 March 2024; revised 16 July 2024; accepted 20 August 2024; published 5 September 2024)

The pursuit of multiferroic magnetoelectrics, combining simultaneous ferroelectric and magnetic orders, remains a central focus in condensed matter physics. Here we report that centrosymmetric, one-dimensional (1D) antiferromagnetic WOI_3 undergoes a strain-induced ferroelectric distortion. The paraelectric-ferroelectric transition is originated from the unconventional anisotropic d^1 mechanism, where an unpaired d electron of each W^{5+} ion contributes to magnetic orders. Employing a Heisenberg model with Dzyaloshinskii-Moriya interaction, we predict an antiferromagnetic spin configuration as the paraelectric ground state, transitioning to a ferroelectric phase with noncollinear spin arrangement under uniaxial strain. The ferroelectric polarization and noncollinear spin arrangement can be manipulated by varying the applied strain. While the energy barriers for switching ferroelectric polarizations with magnetic orders are on the order of a few dozen meV, the shift current bulk photovoltaic effect exhibits remarkable differences, providing a precise and valuable tool for experimentally probing the interplay of ferroelectric and magnetic orders in 1D WOI_3.

DOI: 10.1103/PhysRevB.110.094408

I. INTRODUCTION

Multiferroics have been a focal point in the realm of condensed matter physics [1–6], and are promising to be vastly applied in nonvolatile data storage, sensors, actuators, and so on [6], especially for those materials combining ferroelectricity (FE) and magnetic behaviors [4]. Due to clean surfaces and a large dielectric constant in the miniaturization of the electronic devices [6], low-dimensional [one- (1D) and two-dimensional (2D)] multiferroic materials have attracted significant attention. Based on the mechanism of generating multiferroicity [2,5], multiferroic materials can be classified into type-I (sources of FE and magnetism are independent) and type-II (magnetism causes FE) categories. Notable examples of type-I materials include artificial low-dimensional materials, like halogen-decorated phosphorene bilayers [7]; 2D van der Waals (vdW) heterostructure of $Cr_2Ge_2Te_6$ onto In_2Se_3 [8], etc.; and transition-metal halide monolayers, like $(CrBr_3)_2Li$ [9], while $Hf_2VC_2F_2$ MXene monolayer [10] and few-layer NiI_2 [11] belong to type II.

Type-I multiferroic materials violating the conventional d^0 rule of octahedral distortion for FE by external strain engineering [12,13], and intrinsic anisotropic d^1 rule [14–16] provide the potential for simultaneous magnetic and ferroelectric ordering. Increasing the lattice constants, epitaxial strains, and chemical pressure are discussed in relation to stabilizing the FE state in antiferromagnetic (AFM) materials like $SrMnO_3$ [12] and $BaMnO_3$ [13], respectively. On the other hand, the materials of d^1 configurations, if governed by Hund's rule, exhibit no pseudo-Jahn-Teller effect (PJTE) on dipolar distortion and no ferroelectric instability [17,18], due to the mismatch in spin multiplicities of the lowest unoccupied molecular orbital (LUMO) and the highest occupied molecular orbital (HOMO). Nevertheless, d^1 configurations have not been fully excluded from satisfying the condition of PJTE [18]. The anisotropic d^1 rule was recently proposed in predicting the ground-state FE and AFM orders in the 2D VOX_2 (X = Br, Cl, I) monolayer [14]. Distinct from the conventional d^1 configurations, the anisotropy of the local octahedral field could lead PJTE instability by splitting the threefold degenerate t_{2g}^* molecular orbitals. Additionally, the spiral-spin noncollinear magnetic order is then predicted by introducing the effect of the Dzyaloshinskii-Moriya interaction (DMI) [16].

In this work, we report the strain-induced coexistence of ferroelectricity and antiferromagnetism of the 1D vdW semiconductor WOI_3 based on density functional theory (DFT) calculations. Distinct from the octahedral quasi-1D WOX_4 (X = Br, Cl, I) [19] and 1D WOF_4 [20], in which the intrinsic ferroelectricity is rooted from the electronic d^0 configurations, the 1D WOI_3 material exhibits anisotropic d^1 configuration

*These authors contributed equally to this work.
†Contact author: qijingshan@email.tjut.edu.cn
‡Contact author: daodaohw@zju.edu.cn

despite sharing similar octahedral structures, and is predicted to experience a paraelectric-ferroelectric phase transition under axial tensile strain. Furthermore, the ground-state AFM order is predicted, and the emerging DMI effect, caused by strain-induced FE distortion, could alter the magnetic orientations from collinear configurations to noncollinear configurations. Both the FE polarizations and noncollinearity are monotonically increased with increasing strain. We further explore the shift current bulk photovoltaic effects (BPVEs), which are recognized as the second-order nonlinear optical responses, under varying strains and different ferroelectric and magnetic states in the 1D WOI_3. The shift current is one of the direct BPVE photocurrents that has regained massive attention in both theoretical [21–27] and experimental [28–31] condensed matter physics due to its geometric nature and potential applications [32–34]. It is noteworthy that the synthesis of bulk vdW WOI_3 [35] and other MYX_3's (M = Mo, W; Y = O, S, Se; X = Cl, Br) [36–38], sharing the same crystal structure, was reported decades ago. The synthesis of WOI_3 [35] and other crystals like $MoOBr_3$ [38] is also experimentally feasible, achieved by reactions in sealed ampoule heating at temperatures of several hundred degrees Celsius for a duration from hours to days. Encouraged by the experimental achievements, this work suggests the 1D semiconductor WOI_3 as a promising multitunable platform for nonlinear optics, paving the way for next-generation devices that harness the intricate interplay of electricity and magnetism through nonlinear optical responses.

II. METHODS

Density functional theory (DFT) [39,40] calculations are performed by the Vienna *Ab initio* Simulation Package (VASP) [41,42], which employs the projected augmented-wave (PAW) approach for the core electrons. The generalized gradient approximated (GGA) functionals [43,44] of Perdew-Burke-Ernzerhof (PBE) type parametrization [45] are implemented to consider the exchange-correlation energy of all valence electrons. For vdW bulk WOI_3, the lattice structures are relaxed using the DFT+D2 correction method [46]. Due to strong electronic localization for 5*d* electrons of W atoms, the Hubbard correction with simplification of Dudarev *et al.* [47] is further added to the GGA functionals. The Hubbard parameter $U_{\text{eff}} = U - J = 2$ eV is chosen to embed magnetic moments for W atoms approaching 1 μ_B in DFT calculations (Fig. S8 in the Supplemental Material [48]), which is consistent with the following studies based on the Heisenberg model. Calculations with other values of U_{eff} within $U_{\text{eff}} < 2.5$ eV have been checked, and the conclusions for magnetism of 1D WOI_3 remains the same (Table S1 [48]). The $1 \times 1 \times 2$ supercell of 1D WOI_3 material is mainly used in DFT calculations, allowing for six different magnetic configurations being taken into account. A cutoff energy for the plane-wave basis sets is set as 450 eV, and a $1 \times 1 \times 7$ k-point sampling is used. The DFT results are consistently obtained under the convergence criteria of 1 meV/Å and 1×10^{-6} eV for residual forces in ion relaxations and energy difference between successive self-consistent field (SCF) calculation steps, respectively. In phonon spectrum calculations, supercells with a maximal size of $1 \times 1 \times 8$ are used, and a stricter criterion of 1×10^{-7} eV is applied for SCF.

Based on DFT calculations, the following methods are further conducted to investigate the FE and magnetic orders of WOI_3. The standard Berry phase approach [49] is employed to calculate FE polarizations. The torque method [50,51] is applied for a magnetic anisotropy energy (MAE) profile with an error tolerance of $\sim 0.01\pi$ solid angle. In the Monte Carlo (MC) simulations of the Heisenberg model for WOI_3, the orientations of the magnetic moment are sampled in a supercell of $1 \times 1 \times 2000$ grids to get rid of interference from the boundaries. The MC simulations are performed under a temperature of 10^{-8} K, and the Metropolis algorithm [52] and the Hinzke-Nowak methods [53] are introduced to improve the sampling efficiency. Initial magnetic configurations are deployed randomly, and a dynamic balance of the magnetic moments is reached after 1×10^5 steps.

The Wannier-interpolation scheme [54,55] is employed in calculations for shift current responses. The maximally localized Wannier functions (MLWFs) are obtained iteratively with initial guess constructed by projection functions of W d, I p, and O p orbitals, as implemented in the WANNIER90 code [56]. The tight-binding model is built from the basis set of MLWFs, and the WANNIERBERRI code [57] is then used to calculate the shift current response. Within the calculations, a dense k-point mesh of $1 \times 1 \times 400$ for integrations and a fixed width of 0.025 eV for broadening Dirac δ functions are adapted.

The visualization of the crystal structures are carried out with VESTA software [58]. The output data from the above codes are in units of three-dimensional (3D) systems. The 1D results for shift current response ($\text{nm}^2\,\mu A/\text{V}^2$), linear optical response (pS cm), and FE polarization (pC m) are then obtained by multiplying data with the cross section of 25 Å $\times$ 25 Å.

III. RESULTS

A. Strain-induced ferroelectricity

We start with a brief description about the WOI_3 crystal in the paraelectric (PE) phase. The ladderlike 1D WOI_3 is formed by two 1D chains. Within the chains, highlighted in Fig. 1(a), each tungsten (W) atom is confined in an irregular octahedron four planar iodine atoms (I) and two apical oxygen atoms (O). A $1 \times 1 \times 2$ cell of WOI_3 is used in DFT calculations [Fig. 1(b)]. The crystal structure is built by inserting 17.2 and 21.0 Å vacuum layers over the a and b directions, and is then optimized with a relaxed lattice constant c = 3.825 Å with GGA-level accuracies. The PE structure of WOI_3 is in the space groups *Pmmm* (No. 47) with two W atoms residing in the plane composed of the six planar I atoms. The bulk structure of WOI_3, composed of the ladderlike 1D WOI_3 weakly bound by the vdW interaction, is presented in Fig. S1(a) [48]. A theoretical exfoliation energy of approximately 0.37 J/m^2 is estimated for the bulk (Fig. S1(b) [48]), which is comparable to the calculated exfoliation energy of phosphorene and graphene. Note that mechanically or chemically exfoliating a single or a bundle of 1D structures like WOI_3 still remains challenging [59], and a recent work about quasi-1D $CrSbSe_3$ paves the way for the realization of exfoliation in experiments [60]. The estimated exfoliation energy,

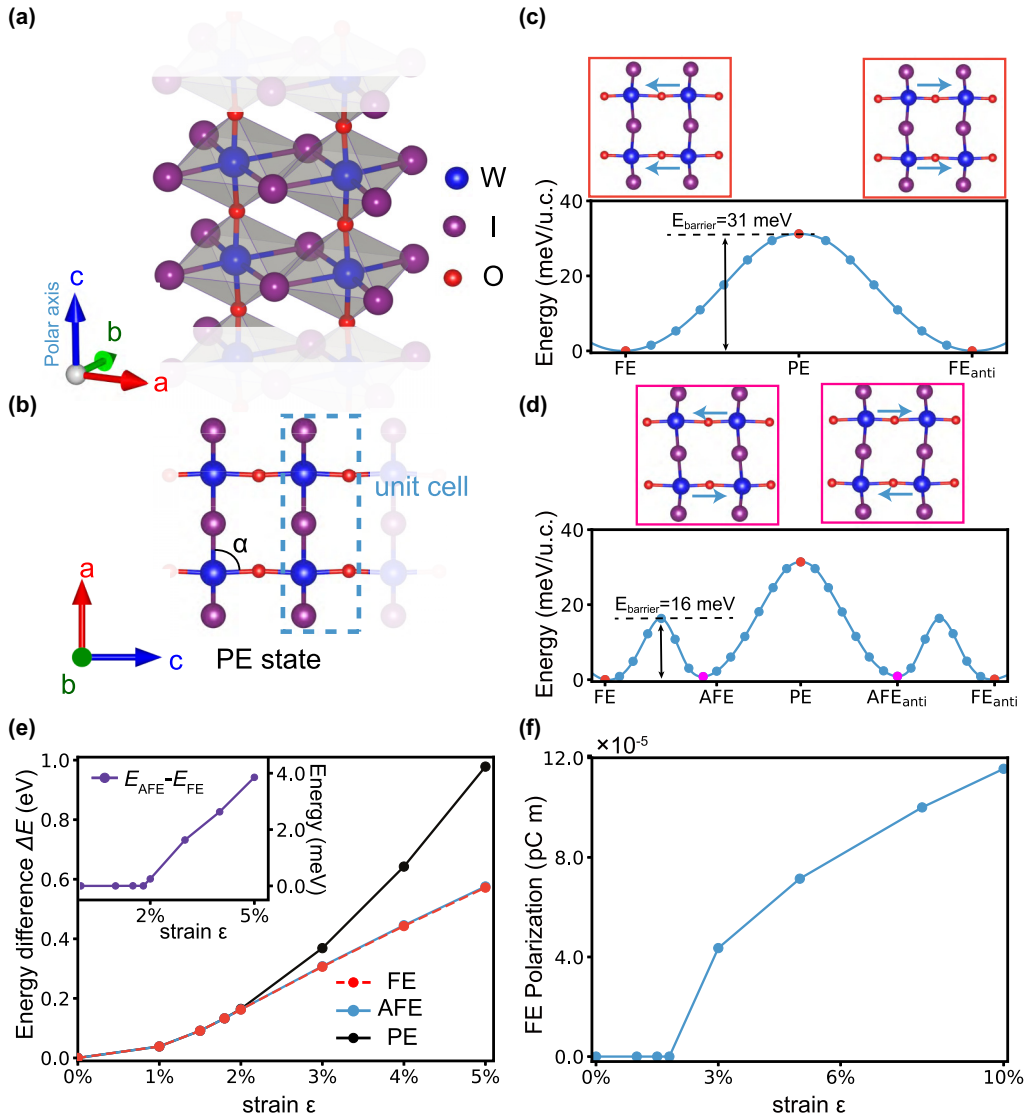

FIG. 1. Crystal structures and ferroelectricity for the 1D WOI_3. The structures of the PE state viewed in (a) the crystal orientation and in (b) the b direction. The ladderlike unit cell is highlighted in the blue dashed box, and the specific O–W–I bond angle α in the lower left corner of the cage of the $1 \times 1 \times 2$ cell characterizes the distortion degree. Under a uniaxial strain of $\varepsilon = 3\%$ along the polar c axis, the adiabatic energy pathways from the nudged elastic band (NEB) are presented for (c) FE-PE-FE_{anti} and (d) FE-AFE-PE-AFE_{anti}-FE_{anti}, with structures of the FE/FE_{anti} and AFE/AFE_{anti} states addressed. Here, the energy barriers of the transition states are labeled. The FE_{anti} represents the FE state with the opposite polarization direction. (e) The energy difference $\Delta E = E - E_{PE,0\%}$ of different states under $\varepsilon = 0\%$–5%, and the energy difference between FE and AFE is presented in the inset. (f) The FE polarization intensity along the periodic direction c axis P_c under different strains.

comparable to other typical low-dimensional materials, indicates that isolating single 1D WOI_3 for theoretical study is rational.

Applying uniaxial tensile strain ε along the c axis, the WOI_3 crystal demonstrates the capability to undergo a PE to FE structural phase transition. The nudged elastic band (NEB) calculations [61,62] under $\varepsilon = 3\%$ yield two adiabatic energy pathways, and the results show that the structure in the FE/FE_{anti} phase is in the ground state [Fig. 1(c)], while the AFE/AFE_{anti} structure is metastable [Fig. 1(d)]. The former belongs to the $Pmm2$ (No. 25) space group with W^{5+} ions for both chains shifting along the same c direction, and the latter is in the $Pm/2$ (No. 31) space group with canceled polarization due to opposite c-direction displacements of W^{5+}. The structure in the FE/FE_{anti} phase is also verified to be stable by phonon spectrum calculations (Fig. S2 [48]). The energy barrier of reversing the FE polarizations in WOI_3 is typically in the range of several dozens of meV/u. c. Specifically, the barrier of the PE state is 31.2 meV/u. c. and barrier between FE and AFE is 16.2 meV/u. c. under a strain of $\varepsilon = 3\%$ [Figs. 1(c) and 1(d)]. Compared with other low-dimensional materials, like 2D α-In_2Se_3 (~850 meV/u. c.) [63], the FE switching in WOI_3 can be easily achieved by applying electric fields.

For varying strain intensity ε, the transitions between the PE, AFE, and FE phases are elucidated by examining the

TABLE I. The energy difference, $\Delta E = E - E_{\mathrm{PE},\,0\%}$ (left panel) and the angle, α, characterizing the magnitude of structure distortion (right panel) for PE, FE, and AFE states under strain $\varepsilon = 0\% - 5\%$.

	ΔE (eV)			α (deg)		
Strain ε	PE	FE	AFE	PE	FE	AFE
0%	0	–	–	88.0972	–	–
1%	0.038583	0.038583	0.038583	88.1990	88.2007	88.2046
1.5%	0.091284	0.091285	0.091288	88.2475	88.2120	88.2250
1.8%	0.132926	0.132926	0.132927	88.2725	88.2360	88.2506
2%	0.164657	0.162495	0.162743	88.2942	86.8346	89.6263
3%	0.368723	0.306299	0.307929	88.4168	84.7014	91.5060
4%	0.642511	0.442843	0.445473	88.4168	83.7014	92.6567
5%	0.978206	0.571920	0.575775	88.4676	82.7923	93.5199

energy differences, $\Delta E = E - E_{\mathrm{PE},0\%}$ [depicted in Fig. 1(e) and summarized in Table I] along with the specific angle α (Table I). Here the angle α refers to the angle at the lower left corner of the cage shown in Fig. 1(b). In the PE state under increasing intensity of strain ε, both ΔE_{PE} and α_{PE} become larger. Under strains of $2\% \leqslant \varepsilon \leqslant 5\%$, the differences between ΔE_{FE} (ΔE_{AFE}) and ΔE_{PE} are significant, and the FE state becomes the lowest-energy state with ΔE_{FE} being smaller than ΔE_{AFE} by a few meV. Regarding structural distortion, the α_{FE}'s for the FE state are consistently smaller than the α_{PE}'s, while the α_{AFE}'s for the AFE state are larger than the α_{PE}'s. With increasing strength of strains, the differences in angles become larger. However, for strains $\varepsilon < 1.8\%$, both α and ΔE of FE, AFE, and PE structures exhibit virtually no difference, which indicates that the PE to FE critical point (CP) may locate near strain $\varepsilon = 1.8\%$. The phase transition is further evident in the FE polarizations depicted in Fig. 1(f), which increases monotonically above the CP strain and vanishes below it. Our prediction of the strain-induced FE phase transition in WOI_3 appears to be highly feasible for experimental validation by hysteresis loop measurements, particularly in light of the spontaneous structure distortions derived in a recent x-ray diffractogram of 1D $MoOBr_3$ [38].

The FE-state property of strained vdW bulk WOI_3 is further studied in Fig. S3 [48]. Four different configurations (Fig. S3(a) [48]), differentiated by the directions of W^{5+} ion shifting along the c axis within 1D chains, are considered. The results in Fig. S3(b) [48] illustrate that the FE-state bulk WOI_3, composed of FE-state 1D WOI_3 with the same directional polarizations, is more stable than other structures with polarization canceling. As with many other low-dimensional materials [59], the properties in vdW bulk WOI_3 such as ferroelectricity can be derived from the 1D character. For researching properties of a material such as strained-induced ferroelectricity, magnetism, and nonlinear optics, the simplicities of 1D structure allow for a clear presentation of the underlying mechanism. From the perspective of application, low-dimensional multiferroic materials have potential benefits for miniaturization and large-scale integrations for electronic devices. Possible implementations of various multiferroic 2D materials, with individual atomic planes, in devices have been reported recently but few in 1D materials [2,5]. This work thus mainly focuses on the studies based on 1D WOI_3.

B. Anisotropic d^1 mechanism

The emergence of ferroelectricity in the strained 1D WOI_3 material could be attributed to the anisotropic d^1 rule. This rule has been recently introduced to elucidate potential multiferroic properties in 2D VOX_2 (X = Cl, Br, I) monolayer. Analysis of spatial charge densities and projected densities of states (PDOS) are conducted, as detailed in Refs. [14–16]. Due to an unpaired d electron of W^{5+} centered at each octahedron, the WOI_3 is a non-d^0 system. We substantiate the applicability of the anisotropic d^1 rule for the strain-induced FE transition in WOI_3 by examining the charge density [Fig. 2(a)] and the PDOS (Figs. 2(b) and S4–S6 in the Supplemental Material [48]). The xy coordinates are clearly marked in Fig. 2(a), and additional information regarding the selected xy coordinates and spin polarizations can be found in Fig. S7 of the Supplemental Material [48]. The degree of coupling between the W d orbital and the O p orbital is elucidated from the spin-polarized PDOS of ($\varepsilon = 0\%$, PE), ($\varepsilon = 3\%$, PE and FE), and ($\varepsilon = 5\%$, PE and FE). With a discernible level of hybridization for the $d_{xz}(d_{yz})$ orbitals and the O p orbital, the coupling between the d_{xy} orbital and the O p orbital remains negligible. The unpaired electrons occupying the d_{xy} orbital [Fig. 2(a)] do not cause significant hindrance when W^{5+} moves along the W-O chain. On the other hand, the spin multiplicity of HOMO and LUMO configurations is illustrated from the PDOS of the spin-up unit cell [Fig. 2(b)]. Near the Fermi energy, the spin-up PDOS of the occupied d_{xy} orbital indicates the HOMO configuration as $(t_{1u})^6(d_{xy}\uparrow)^1$. The observable spin-down PDOS of unoccupied $d_{xz}(d_{yz})$ orbitals informs a possible configuration of $(t_{1u})^5(d_{xy}\uparrow)^1(d_{yz}\downarrow + d_{xz}\downarrow)^1$ for LUMO, which shares the same spin multiplicity as HOMO.

With hindrance-free d_{xy} electrons and the same spin multiplicities, the anisotropic d^1 configuration bears a resemblance to the conventional d^0 configuration, and the HOMO and LUMO can hybridize under the polar displacement of W^{5+} along the W-O bonds leading to finite vibronic coupling, $F \neq 0$. The occurrence of PJTE instability depends on whether the vibronic-coupling contribution, $K_V \approx -2|F|^2/(\Delta E_{\mathrm{LUMO-HOMO}})$, is sufficient enough to overcome the lattice stiffness, K_0. In the pristine WOI_3 ($\varepsilon = 0\%$), the vibronic-coupling contribution might not be dominant due to

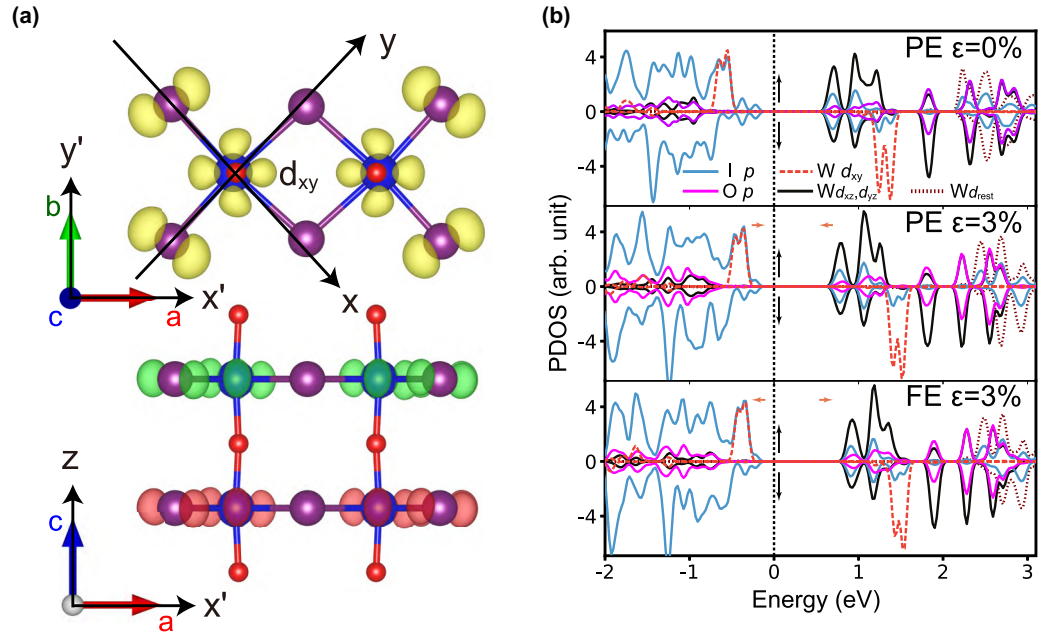

FIG. 2. Spatial charge densities and spin-polarized PDOS in supporting the ferroelectric anisotropic d^1 rule. (a) The charge densities represented by red (spin-up), green (spin-down), and yellow (both) isosurfaces with isosurface level of 3×10^{-11} e/bohr^3. The charge densities localized at W atoms correspond to the occupied d_{xy} orbitals. Here, the xy coordination axes for the orbitals are set to be aligned with the I-W bonds, distinguished from the marked $x'y'$ coordination axes. (b) The spin-up and spin-down PDOS for ($\varepsilon = 0\%$, PE), ($\varepsilon = 3\%$, PE), and ($\varepsilon = 3\%$, FE) are presented within the near-gap energy region. The red dashed and black solid lines represent the PDOS of d_{xy} and $d_{xz} + d_{yz}$ orbitals for W atoms, while the brown dotted lines are PDOS for the rest of the orbitals of W atoms. The p orbitals of I and O atoms are, respectively, denoted by blue and magenta solid lines.

a large HOMO-LUMO gap, $\Delta E_{\mathrm{LUMO-HOMO}}$, and the ground-state structure is in PE under $K_0 + K_V > 0$. When applying tensile strains ($\varepsilon > 1.8\%$) to elongate the W-O bonds, the decrease of $\Delta E_{\mathrm{LUMO-HOMO}}$, implied by the reduction of the energy gap of ($\varepsilon = 3\%$, PE) [Fig. 2(b)], leads to an augmentation for the vibronic-coupling contribution, K_V. The FE polarization can then occur triggered by the PJTE instability with $K_0 + K_V < 0$. The HOMO state of distorted WOI_3, derived from the hybridization of the HOMO and LUMO states of ($\varepsilon = 3\%$, PE), is eventually restabilized with an enlarged HOMO-LUMO gap, which is confirmed by the expanded energy gap of ($\varepsilon = 3\%$, FE) [Fig. 2(b)].

C. Strain-tuning noncollinear antiferromagnetism

Next we turn to the magnetic property of WOI_3 arising from the extra unpaired d electrons of W^{5+}. To explore the influence from the strain-induced FE distortion onto ground-state magnetic configurations, we include spin-orbit couplings (SOCs) in DFT calculations, and then conduct MC simulations (see the Methods section) based on the effective Heisenberg model [64].

In the Heisenberg model, effective magnetic moments of atoms are incorporated for the study of macroscopic magnetic order. Both the magnitudes and directional dependence of atomic magnetic moments are carefully checked as follows to ensure a rational modeling. The magnitude of the magnetic moment of W^{5+} is approximately 1.10 μ_B, obtained by integrating spin charge density within the effective radius in VASP. The magnetic moments of I^- and O^{2-} range within $0.01 - 0.04$ μ_B, varying with distance from W^{5+}. These values align with the expected magnetic moments, considering the presence of one extra unpaired d electron of W^{5+} and four spin pairings of I^- and O^{2-}, with small deviations due to covalent bonding. The magnetic moments remain consistent under different strain magnitude in our DFT calculations. The influence of the Hubbard correction under different U_{eff}'s on the magnitude of the magnetic moment of W^{5+} are also inspected, and $U_{\mathrm{eff}} = 2$ eV is chosen in this work to embed magnetic moments with strength approaching ideal values (Fig. S8 and Table S1 in the Supplemental Material [48]). According to the Mermin-Wagner theorem [65], directional isotropy for spins causes strong fluctuations to prohibit spontaneous symmetry broken in 1D and 2D spin systems. In magnetic ordered materials, like $CrSbSe_3$ studied in our previous work [66], magnetic anisotropy plays a key role in the suppression of such spin fluctuations. To demonstrate magnetic anisotropy of WOI_3, we perform MAE calculations for the 3D energy profile by rotating the atomic magnetic moments over the entire space under $\varepsilon = 0\%$ [Fig. 3(a)], and maintain opposing magnetic moments in neighboring unit cells [labeled as AFM 1; see Fig. 3(c)]. The substantial magnetic anisotropy of WOI_3 is evident from the MAE profile. Thus, within the Heisenberg model, the strength of magnetic moments localized at W sites is treated as constant (approximately 1 μ_B), and magnetic anisotropy is considered. Additionally, we determine the energetically favorable easy axis by careful numerical examinations with an error tolerance of 0.01π in the solid angle, which lies at an angle of 43.20° with respect to the a axis and 62.61° for the c axis. The hard axis stays at angles

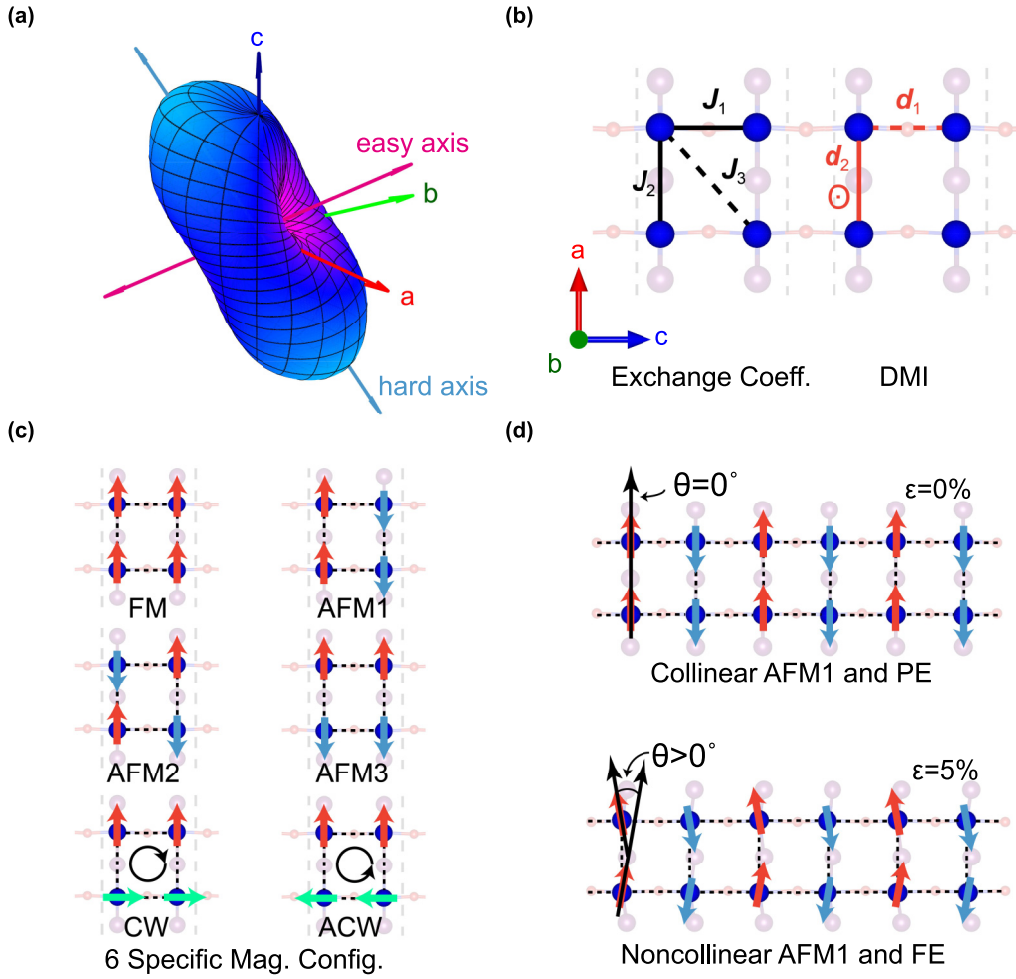

FIG. 3. MAE surface and schematics of Heisenberg models and magnetic configurations. (a) The MAE surface of the 1D WOI_3 with easy axis (red) and hard axis (blue). (b) The schematic diagrams for the exchange coefficients and DMI vectors considered in the anisotropic Heisenberg model. (c) Six specific magnetic configurations used in determining parameters of the anisotropic Heisenberg model. These configurations are collinear ferromagnetic (FM) order and three kinds of antiferromagnetic (AFM 1–3) orders, and noncollinear clockwise (CW) and anticlockwise (ACW) configurations. (d) Schematic diagrams for the magnetic configurations under strain of $\varepsilon = 0\%$ and $\varepsilon = 5\%$. The red and blue represent the magnetic moments at sites of the W atom in a ladderlike unit cell, and the averaged intersection angle θ is introduced to characterize the degrees of the noncollinearity.

of (230.40°, 32.86°). These spin orientations hold for various strains less than $\varepsilon = 10\%$, as confirmed by DFT calculations with the same error tolerance, demonstrating the stability of the easy axis orientation across different strains.

Based on the aforementioned insights, we introduce the general Heisenberg Hamiltonian,

$$H = \sum_{i\neq j}\sum_{\alpha=(a,b,c)}\left[J_{i,j;\alpha}s_i^\alpha s_j^\alpha + d_{i,j;\alpha}(\mathbf{s}_i\times\mathbf{s}_j)^\alpha\right] + \sum_i\sum_{\alpha=(a,b)} D_{i;\alpha}\left(s_i^\alpha\right)^2, \quad (1)$$

governing the collective behavior of the fixed-strength magnetic moments at W^{5+} sites, denoted by $\boldsymbol{s}_i = \{s_i^\alpha\}(\alpha = a, b, c)$. The magnetic anisotropy is addressed by the subscript α for all the coefficients in Eq. (1), including the single-ion anisotropy coefficient, $D_{i;\alpha=(a,b)}$. For the PE structure (space group *Pmmm*), the asymmetric DMI of magnetic moments of 1D WOI_3 is zero due to inversion symmetry. However, when strain ε (>1.8%) is applied, the FE deformation leads inversion symmetry breaking. Within a unit cell, a mirror plane includes both W^{5+}'s and transects the W-I_2-W structure along the *ac* plane. According to Moriya's rules [67,68], finite DMI could be expected for FE structure, with the DMI coefficient vector being along the *b* direction, $d_{i,j;\alpha=b}$. To estimate the strain effect on magnetic noncollinearity, the DMI term with $d_{i,j;\alpha}$, is included in Eq. (1) for each pairing site of $\{i, j\}$. Here, $J_{i,j;\alpha}$ represents the anisotropic exchange coefficient. Reasonable simplifications and truncations are further introduced in Eq. (1) to make MC simulations numerically feasible. The subscript i of the single-ion anisotropy coefficients $D_{i;\alpha}$ is omitted by assuming homogeneity for all W^{5+} sites, and the coefficients are collectively denoted as $\boldsymbol{D}$. As shown in Fig. 3(b), the nearest-neighboring (NN) terms of Eq. (1) are mainly considered with NN exchange coefficient vectors, $\{\boldsymbol{J}_1, \boldsymbol{J}_2\}$, and NN DMI coefficient vectors, $\{\boldsymbol{d}_1, \boldsymbol{d}_2\}$. An additional next-nearest-neighboring (NNN) exchange term

TABLE II. The results of NN exchange coefficients and DMI, J_1, J_2, and $d_{2;b}$, for the anisotropic Heisenberg model and the averaged intersection angle θ under strains of $\varepsilon = 0\% - 10\%$.

Strain ε		J_1	J_2 (meV/μ_B^2)	$d_{2;\alpha=b}$	θ (deg)
0%	a	1.07(2)	−4.28(8)	0	0
	b	0.79(4)	−4.50(9)		
	c	1.18(6)	−4.44(5)		
3%	a	0.85(9)	−3.98(1)	0.49 (5)	5.69(2)
	b	0.63(9)	−3.81(5)		
	c	0.95(6)	−4.13(2)		
5%	a	0.72(5)	−3.77(3)	0.62(3)	7.36(5)
	b	0.60(5)	−3.15(9)		
	c	0.77(4)	−3.92(6)		
8%	a	0.49(8)	−3.57(7)	0.91(9)	10.91(8)
	b	0.45(8)	−2.66(8)		
	c	0.51(1)	−3.75(7)		
10%	a	0.40(4)	−3.58(3)	0.98(0)	11.68(6)
	b	0.37(1)	−2.59(6)		
	c	0.41(5)	−3.76(9)		

with $\boldsymbol{J}_3$ is also included to account for the minority of longer-range terms.

The coefficients $\boldsymbol{J}_{k(=1,2,3)}$, $\boldsymbol{d}_{k(=1,2)}$, and $\boldsymbol{D}$ are determined by six kinds of specific magnetic configurations [Fig. 3(c)]. Among these configurations, there are four collinear configurations, including FM, AFM 1, AFM 2, and AFM 3. Two additional noncollinear configurations have clockwise (CW) and anticlockwise (ACW) orientations. The total energy from DFT calculations for the six configurations are listed with different magnetic anisotropy ($\alpha = a, b, c$) and different strains ε in Table S2 of the Supplemental Material [48]. For each anisotropic direction α, the determination of $J_{k(=1,2,3);\alpha}$ and D_α involves linear equations formed by Eq. (1), which parametrizes $s_i^\alpha s_j^\alpha$ and $(s_i^\alpha)^2$ (first column in Table S2 [48]). The values of $\boldsymbol{d}_{k(=1,2)}$ are subsequently determined by solving linear equations built from the remaining two noncollinear configurations. The determination process is repeated for various strains ε ($\leqslant 10\%$). The NN parameters are listed in Table II, and the results for $\boldsymbol{J}_3$ and $\boldsymbol{D}$ can be found in Table S3 [48]. Given that the values of NNN $\boldsymbol{J}_3$ are approximately two orders of magnitude smaller than NN $\boldsymbol{J}_{k=1,2}$, the effects of exchange interactions from longer-than-NN sites are expected to be minor. Notably, $d_{2;b}$ is finite, while other NN DMI coefficients remain negligible under different strains ε ($\geqslant 3\%$), which agrees with the predictions from Moriya's rules.

For the collinear magnetic configuration under each strain ε, the AFM 1 configuration is suggested to be the lowest-energy magnetic order, due to the positive $\boldsymbol{J}_1$ and negative $\boldsymbol{J}_2$. Note that this ground-state magnetic configuration remains the same under different values of Hubbard parameters as shown in Table S1 [48]. As the FE distortion intensifies, the enhancement of noncollinearity is implied from the increase of the DMI $d_{2;b}$. To manifest the impact of noncollinearity within the 1D crystal model, the MC simulations based on Eq. (1) are then conducted to investigate the ground-state noncollinear magnetic configurations. According to the simulation results, the parallel magnetic moment vectors in the lth unit cell within PE structure are expanded with an intersection angle, θ_l, along the a direction under the effect of FE distortion [as schematically shown in Fig. 3(d)]. The growing noncollinearity with increasing strain ε is quantitatively characterized by the statistical average angle, $\theta = \langle\theta_l\rangle$, which is listed in Table II.

Summarizing the complex phase behaviors around the CP strain $\varepsilon = 1.8\%$, we present a semischematic phase diagram delineating FE, AFE, and PE states in the Supplemental Material [48]. Each phase is highlighted by discernible differences in the structural distortion, the FE polarization, and the magnetic noncollinearity. It is essential to note that this phase diagram representation is just one of several possible configurations. Establishing of a more accurate phase diagram would require sophisticated calculations and even experimental measurements, which lie beyond the scope of this work.

D. Strain-induced shift current BPVE

Finally, we demonstrate the nonlinear optical (NLO) responses, specifically the shift current BPVE under varying strain ε and different ferroelectric and magnetic states for the 1D WOI_3 material. As depicted in the schematic diagram [Fig. 4(a)], these three key factors in tuning the shift current response can be utilized in the future 1D WOI_3-based NLO devices.

The formulation of the NLO response for shift current is briefly summarized here, with detailed derivations available in Refs. [21–24]. In this work, we focus on the z-direction shift current induced by z-polarized light, expressed as $J_{\mathrm{sh};z} = 2\sigma^{z;zz}(\omega)E(\omega)E(-\omega)$, and the shift current conductivity $\sigma^{z;zz}(\omega)$ is formulated as follows:

$$\sigma^{z;zz}(\omega) = -\frac{i\pi e^3}{2\hbar^2}\int_{\mathrm{BZ}}\left(\frac{\mathrm{d}k}{2\pi}\right)\sum_{n\neq m} f_{mn}\mathrm{Im}(r_{nm;z}r_{mn})\delta(\omega-\omega_{nm}). \tag{2}$$

Here, the difference for the Dirac-Fermi distributions and energies between bands n and m are denoted by f_{nm} and ω_{nm}, respectively, and the summation in Eq. (2) runs over pairs of valence and conduction bands. For each n, m band, the dipole moment is given by the interband Berry connections, $r_{nm}(k) = i\langle n|\partial_k|m\rangle$, and its covariant derivative is defined as $r_{nm;z}(k) = \partial_k r_{nm} - i[A_n(k) - A_m(k)]r_{nm}$. The intraband Berry connection of the n band is denoted as $A_n = i\langle n|\partial_k|n\rangle$. Here $|n\rangle$ and $|m\rangle$ denote the cell-periodic Bloch states.

Based on the calculations of Eq. (2), the impact from strain engineering and FE distortion on the shift current response is explored [Fig. 4(b)]. While maintaining WOI_3 in the FE and collinear AFM 1 state, abbreviated as (FE, AFM 1), the calculations of $\sigma^{z;zz}$ have been performed under different strain conditions, specifically, $\varepsilon = 0\%$, 2%, 3%, and 5% [Fig. 4(b)]. For concise comparison, the frequency axes of the $\sigma^{z;zz}$ are rescaled by subtracting the band gap energy, $\omega - \omega_{\mathrm{gap}} \to \omega$, where $\omega_{\mathrm{gap}} = 0.79$, 0.88, 1.02, and 1.22 eV. Without any strain ($\varepsilon = 0\%$), the shift current response vanishes due to the inversion symmetry, though a finite dipole leads to a finite linear optical response [48]. Within the frequency range of $\omega = [0,\ 0.6]$ eV, the overall profiles of oscillatory shift current responses become larger with increasing frequency for

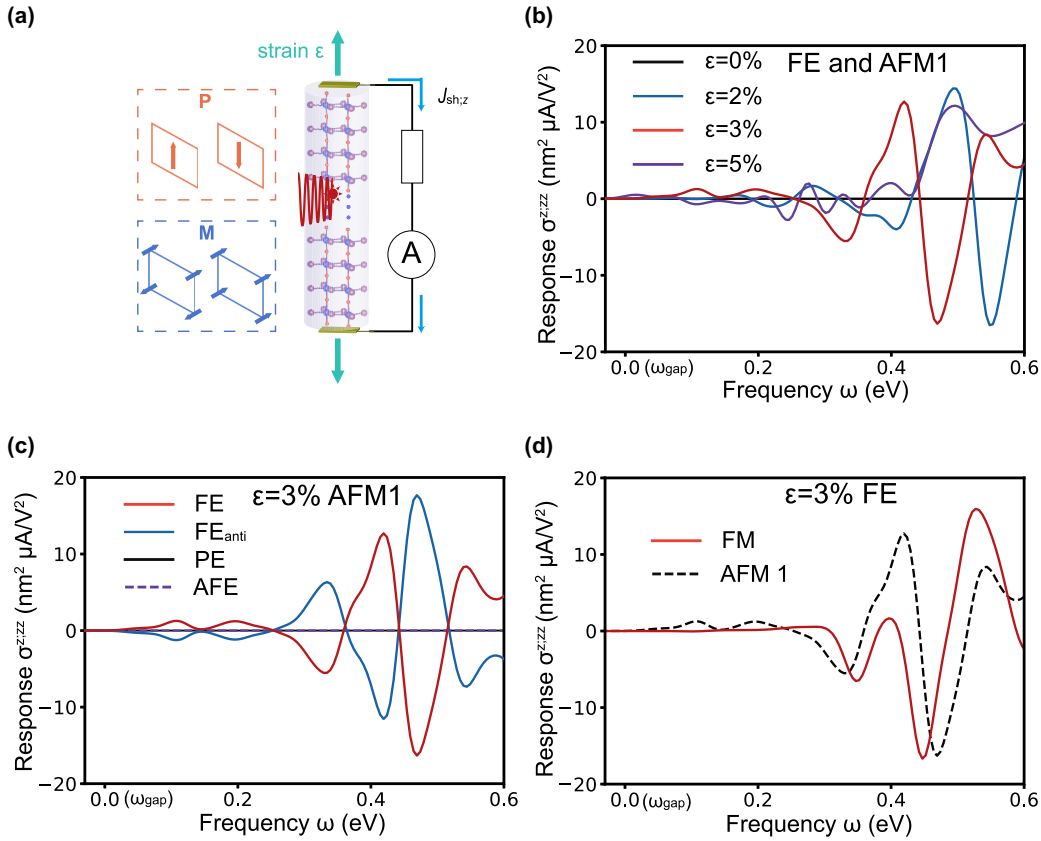

FIG. 4. Shift current response for 1D WOI_3. (a) The schematic diagram for the WOI_3-based NLO device. Within the device, applying tensile strain of $\varepsilon \geqslant 2\%$ triggers the emergence of shift current; different strengths of strain can tune the strengths of the current (green arrows). The modulation onto shift current can be further achieved by altering the direction of FE polarization (brown dashed box) and transitioning the collinear AFM 1 to the FM magnetic phase (blue dashed box). The shift current responses $\sigma^{z;zz}(\omega)$ for (b) the (FE, AFM 1) state under $\varepsilon = 0\%$, 2%, 3%, and 5% represented by black, blue, red, and purple lines; (c) the FE, FE_{anti}, PE, and AFE structures with AFM 1 under $\varepsilon = 3\%$ represented by red, blue, black solid, and purple dashed lines; (d) the FE structure with AFM 1 and FM phases under $\varepsilon = 3\%$ denoted by black dashed and red solid lines. The collinear magnetic orientation is along the easy axis in (b)–(d).

different finite strains, and the increasing trend can also be inspected in linear optical response [48]. The enhancement in large frequencies is originated from the augmentation of transition strength $|r_{nm}(k)|^2$ among deep bands. As shown in the band structure [Fig. 5(a)] and k-resolved shift current response [Fig. 5(c)] under $\varepsilon = 3\%$, the near-gap shift current response mainly arises from the weak C_{2v}-symmetry-allowed transitions between the valence band maximum (VBM) featured with I p_z orbitals at the Γ point and conduction band [I p_z and W $(d_{x'z} + d_{y'z})$ orbitals]. When the light frequency increases, the results of k-resolved shift current response indicate that the pronounced transitions at the k points of $\Gamma \rightarrow \pm Z$ gradually become the primary contribution [Fig. 5(c)], where the components of the flat valence bands turn out to be W $d_{x'^2-y'^2}$ orbitals [Fig. 5(a)]. Note that the $x'y'$ coordinates are marked in Fig. 2(a). As ε increases, the flat valence bands are lifted close to the VBM (see Figs. S11–S14 in the Supplemental Material [48]), and the profiles of the linear optical responses are brought forward [48]. However, within the frequency range of $\omega = [0,\ 0.6]$ eV, the shift current response under $\varepsilon = 3\%$ emerges as an optimal choice, reaching a maximum of about 16 nm^2 μA/V^2 at a rescaled frequency of $\omega_{max} = 0.47$ eV. When yielding comparable strength of shift current responses, ω_{max} 's of $\varepsilon = 2\%$ and 5% are larger than $\varepsilon = 3\%$. The effect of the FE distortion is then investigated from the shift current responses across changing ferroelectric states including results for the PE, AFE, FE, and FE_{anti} states under $\varepsilon = 3\%$ [Fig. 4(c)]. Here the magnetic configuration of WOI_3 consistently follows the collinear AFM 1 order. In the FE_{anti} state, flipping the direction of the FE polarization reverses the sign of $r_{nm;z}$, and the shift current response of the FE_{anti} state is the opposite of the FE state. By contrast, the shift current responses of the PE and AFE states vanish due to inversion symmetry. Applying strains and coercive fields can be utilized to act as on-off and directional switches for NLO-based devices.

The influence of the magnetic properties on shift current response is then explored by changing the magnetic configurations while maintaining the 1D WOI_3 in the FE state under $\varepsilon = 3\%$. When transitioning collinear AFM 1 to FM phase, the near-gap shift current response $\sigma^{z;zz}$ is shifted to a higher light frequency [Fig. 4(d)]. This altering of response arises from the change in $|r_{nm}(k)|^2$, as supported by additional information from the k-resolved shift current response [Fig. 5(d)] and linear optical response (see Fig. S7(b) [48]). The splitting of doubly degenerate bands noticeably reduces the densities

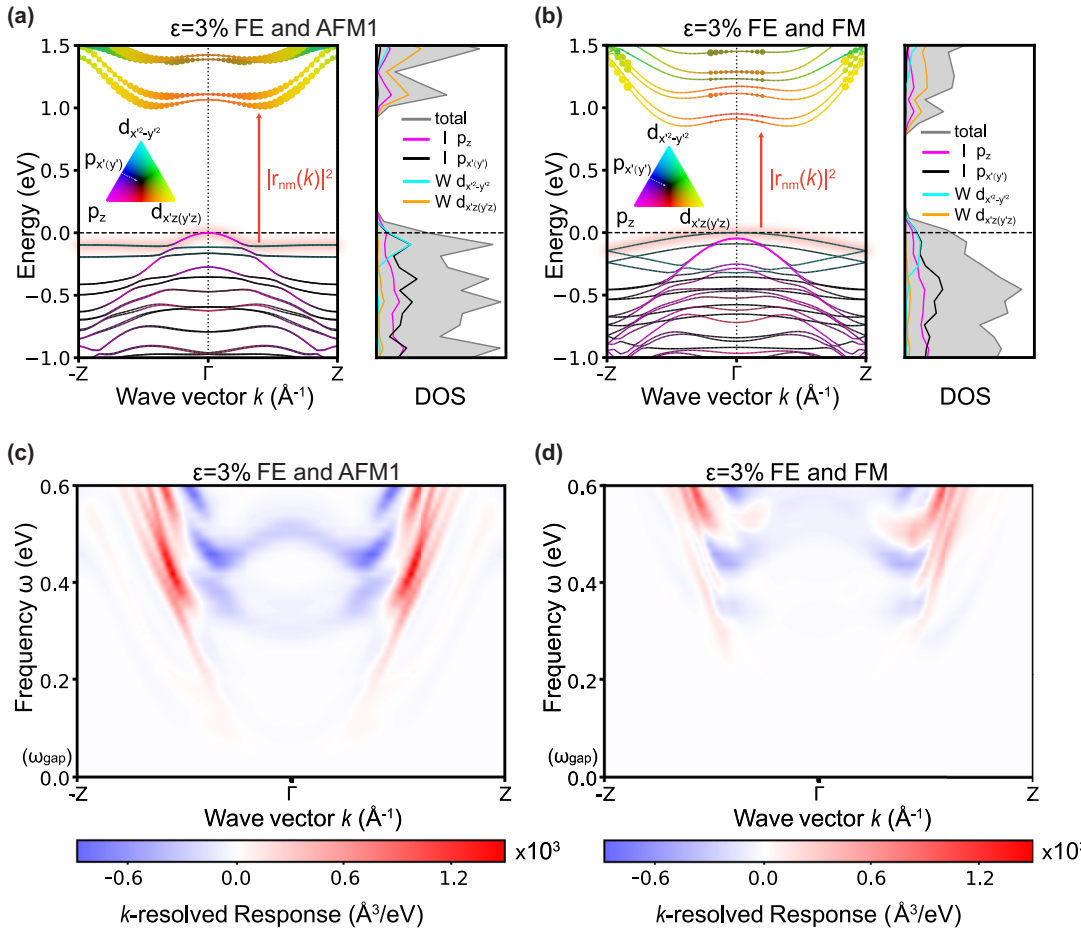

FIG. 5. Band structures and k-resolved shift current response for 1D WOI_3. The band structures and densities of states (DOS) of the (a) (FE, AFM 1) and (b) (FE, FM) states under $\varepsilon = 3\%$. The color composition for each point of orbital projection in bands, using colors (yellow, cyan, black, and magenta), indicates the proportions of W $d_{x'z} + d_{y'z}$, W $d_{x'^2-y'^2}$, I $p_{x'} + p_{y'}$, and I p_z orbitals. The sizes of the solid circles represent the strength of transition dipole moments, $|r_{nm}(k)|^2$, from first gap-edge valence band to conduction bands. The total DOS and orbital PDOS are denoted by gray shaded line and colored lines, respectively. The k-resolved shift current responses of the (c) (FE, AFM 1) and (d) (FE, FM) states under $\varepsilon = 3\%$ are plotted with k points and light frequencies.

of states (DOS) of the gap-edge energy regions (Figs. 5(a) and 5(b) and S15 [48]), and the optical selection rule dominates the suppression of transitions from the gap-edge valence band at the k points of the valleys of the conduction bands [Fig. 5(b)]. Both effects then diminish the gap-edge transitions $|r_{nm}(k)|^2$ for FM order leading to the altering of the shift current response. Additionally, the strain-induced magnetic noncollinearity is found to have a negligible effect on the shift current response [48], while the changes of behavior of the shift current response are minor when altering the direction of the magnetic moments of WOI_3 from the easy axis to the a axis. It aligns with the expectation that changing magnetic orders is more pronounced than fine-tuning magnetic configurations on the electronic structures.

IV. DISCUSSIONS

In this work, we report theoretical investigations of the 1D vdW WOI_3. A strain-induced paraelectric-ferroelectric phase transition is predicted with critical point of strain $\varepsilon_{CP} \sim 1.8\%$ for this material. Our calculations identify WOI_3 as a 1D ferroelectric-antiferromagnetic (multiferroic) semiconductor by strain engineering, where the magnetic moments are originated from the unpaired d_{xy} electrons in the d^1 configuration of the tungsten atoms. The strain-induced FE distortions ($3\% \leqslant \varepsilon \leqslant 10\%$) can also lead to 5°–12° noncollinear tilting of the magnetic moments, pristinely parallel to the easy axis ($\varepsilon = 0\%$), along the direction of the FE polarization. Subsequently, we explore the ferroelectric and magnetic properties concerning shift current BPVE in 1D WOI_3. Strains and electric fields serve as efficient controls for on-off and direction switching of NLO responses. Additionally, changing the magnetic order has been identified as a way to manipulate NLO response. This opens the door for designing advanced optical devices with tailored properties.

We rationalize the multiferroicity in 1D vdW WOI_3 from the anisotropic d^1 rule, as proposed in works concerning 2D $VOX_2 (X = \text{Cl, Br, I})$ [14,15]. The scarcity of systematic investigations into the anisotropic d^1 configuration in generating FE distortion and its implications in designing novel electromagnetic materials remains a significant gap in our understanding. This work paves the way for the discovery of alternative anisotropic d^1 materials, offering insights for the theoretical development of the anisotropic d^1 rule.

Furthermore, 1D vdW WOI_3 is expected to be a multitune platform for devices utilizing shift current BPVE. The efficient control of shift current through the application of strains, external electric fields, and magnetic field is promising for potential applications in NLO devices. Due to the feasibility of synthesis of the bulk vdW WOI_3 [35] and other similar structures [36–38], experimental verifications and applications in NLO devices could be achieved in the foreseeable future.

ACKNOWLEDGMENTS

H.W. and J.Q. acknowledge the support provided by National Natural Science Foundation of China (NSFC) under Grants No. 12304049 and No. 11974148. The work was carried out at the National Supercomputer Center in Tianjin, and the calculations were performed on TianHe-1(A). Z.G. acknowledges Prof. Mingwen Zhao and Mr. Haoqiang Ai for useful discussions.

[1] D. I. Khomskii, Multiferroics: Different ways to combine magnetism and ferroelectricity, J. Magn. Magn. Mater. **306**, 1 (2006).

[2] D. Khomskii, Classifying multiferroics: Mechanisms and effects, Physics **2**, 20 (2009).

[3] M. Fiebig, T. Lottermoser, D. Meier, and M. Trassin, The evolution of multiferroics, Nat. Rev. Mater. **1**, 16046 (2016).

[4] N. A. Spaldin and R. Ramesh, Advances in magnetoelectric multiferroics, Nat. Mater. **18**, 203 (2019).

[5] T. Hu and E. Kan, Progress and prospects in low-dimensional multiferroic materials, Wiley Interdiscip. Rev. Comput. Mol. Sci. **9**, e1409 (2019).

[6] X. Tang and L. Kou, Two-dimensional ferroics and multiferroics: Platforms for new physics and applications, J. Phys. Chem. Lett. **10**, 6634 (2019).

[7] Q. Yang, W. Xiong, L. Zhu, G. Gao, and M. Wu, Chemically functionalized phosphorene: Two-dimensional multiferroics with vertical polarization and mobile magnetism, J. Am. Chem. Soc. **139**, 11506 (2017).

[8] Y. Lu, R. Fei, X. Lu, L. Zhu, L. Wang, and L. Yang, Artificial multiferroics and enhanced magnetoelectric effect in van der Waals heterostructures, ACS Appl. Mater. Interfaces **12**, 6243 (2020).

[9] C. Huang, Y. Du, H. Wu, H. Xiang, K. Deng, and E. Kan, Prediction of intrinsic ferromagnetic ferroelectricity in a transition-metal halide monolayer, Phys. Rev. Lett. **120**, 147601 (2018).

[10] J.-J. Zhang, L. Lin, Y. Zhang, M. Wu, B. I. Yakobson, and S. Dong, Type-II multiferroic $Hf_2VC_2F_2$ MXene monolayer with high transition temperature, J. Am. Chem. Soc. **140**, 9768 (2018).

[11] H. Ju, Y. Lee, K.-T. Kim, I. H. Choi, C. J. Roh, S. Son, P. Park, J. H. Kim, T. S. Jung, J. H. Kim, K. H. Kim, J.-G. Park, and J. S. Lee, Possible persistence of multiferroic order down to bilayer limit of van der Waals material NiI_2, Nano Lett. **21**, 5126 (2021).

[12] J. W. Guo, P. S. Wang, Y. Yuan, Q. He, J. L. Lu, T. Z. Chen, S. T. Yang, Y. J. Wang, R. Erni, M. D. Rossell, V. Gopalan, H. J. Xiang, Y. Tokura, and P. Yu, Strain-induced ferroelectricity and spin-lattice coupling in $SrMnO_3$ thin films, Phys. Rev. B **97**, 235135 (2018).

[13] H. Sakai, J. Fujioka, T. Fukuda, D. Okuyama, D. Hashizume, F. Kagawa, H. Nakao, Y. Murakami, T. Arima, A. Q. R. Baron, Y. Taguchi, and Y. Tokura, Displacement-type ferroelectricity with off-center magnetic ions in perovskite $Sr_{1-x}Ba_xMnO_3$, Phys. Rev. Lett. **107**, 137601 (2011).

[14] H. Tan, M. Li, H. Liu, Z. Liu, Y. Li, and W. Duan, Two-dimensional ferromagnetic-ferroelectric multiferroics in violation of the d^0 rule, Phys. Rev. B **99**, 195434 (2019).

[15] H. Ai, X. Song, S. Qi, W. Li, and M. Zhao, Intrinsic multiferroicity in two-dimensional $VOCl_2$ monolayers, Nanoscale **11**, 1103 (2019).

[16] N. Ding, J. Chen, S. Dong, and A. Stroppa, Ferroelectricity and ferromagnetism in a VOI_2 monolayer: Role of the Dzyaloshinskii-Moriya interaction, Phys. Rev. B **102**, 165129 (2020).

[17] I. B. Bersuker, Pseudo Jahn-Teller origin of perovskite multiferroics, magnetic-ferroelectric crossover, and magnetoelectric effects: The $d^0 - d^{10}$ problem, Phys. Rev. Lett. **108**, 137202 (2012).

[18] I. B. Bersuker, *The Jahn-Teller Effect*, Paperback ed. (Cambridge University Press, Cambridge, 2010).

[19] L.-F. Lin, Y. Zhang, A. Moreo, E. Dagotto, and S. Dong, Quasi-one-dimensional ferroelectricity and piezoelectricity in WOX_4 halogens, Phys. Rev. Mater. **3**, 111401(R) (2019).

[20] T. Xu, J. Zhang, C. Wang, X. Wang, T. Shimada, J. Wang, and H. Yang, Intrinsic ferroelectrics and carrier doping-induced metallic multiferroics in an atomic wire, J. Mater. **9**, 892 (2023).

[21] R. von Baltz and W. Kraut, Theory of the bulk photovoltaic effect in pure crystals, Phys. Rev. B **23**, 5590 (1981).

[22] B. I. Sturman and V. M. Fridkin, *Photovoltaic and Photorefractive Effects in Noncentrosymmetric Materials* (Routledge, Milton Park, UK, 2021).

[23] J. E. Sipe and A. I. Shkrebtii, Second-order optical response in semiconductors, Phys. Rev. B **61**, 5337 (2000).

[24] S. M. Young and A. M. Rappe, First principles calculation of the shift current photovoltaic effect in ferroelectrics, Phys. Rev. Lett. **109**, 116601 (2012).

[25] A. Strasser, H. Wang, and X. Qian, Nonlinear optical and photocurrent responses in Janus MoSSe monolayer and MoS_2-MoSSe van der Waals heterostructure, Nano Lett. **22**, 4145 (2022).

[26] H. Wang, X. Tang, H. Xu, J. Li, and X. Qian, Generalized Wilson loop method for nonlinear light-matter interaction, npj Quantum Mater. **7**, 61 (2022).

[27] A. M. Cook, B. M. Fregoso, F. de Juan, S. Coh, and J. E. Moore, Design principles for shift current photovoltaics, Nat. Commun. **8**, 14176 (2017).

[28] M. Nakamura, S. Horiuchi, F. Kagawa, N. Ogawa, T. Kurumaji, Y. Tokura, and M. Kawasaki, Shift current photovoltaic effect in a ferroelectric charge-transfer complex, Nat. Commun. **8**, 281 (2017).

[29] J. Ma, Q. Gu, Y. Liu, J. Lai, P. Yu, X. Zhuo, Z. Liu, J.-H. Chen, J. Feng, and D. Sun, Nonlinear photoresponse of type-II Weyl semimetals, Nat. Mater. **18**, 476 (2019).

[30] A. M. Burger, R. Agarwal, A. Aprelev, E. Schruba, A. Gutierrez-Perez, V. M. Fridkin, and J. E. Spanier, Direct observation of shift and ballistic photovoltaic currents, Sci. Adv. **5**, eaau5588 (2019).

[31] H. Hatada, M. Nakamura, M. Sotome, Y. Kaneko, N. Ogawa, T. Morimoto, Y. Tokura, and M. Kawasaki, Defect tolerant zero-bias topological photocurrent in a ferroelectric semiconductor, Proc. Natl. Acad. Sci. USA **117**, 20411 (2020).

[32] L. Z. Tan, F. Zheng, S. M. Young, F. Wang, S. Liu, and A. M. Rappe, Shift current bulk photovoltaic effect in polar materials—hybrid and oxide perovskites and beyond, npj Comput. Mater. **2**, 16026 (2016).

[33] Y. Zhou, Y. Huang, X. Xu, Z. Fan, J. B. Khurgin, and Q. Xiong, Nonlinear optical properties of halide perovskites and their applications, Appl. Phys. Rev. **7**, 041313 (2020).

[34] Y. Dang and X. Tao, Recent progress of bulk photovoltaic effect in acentric single crystals and optoelectronic devices, Matter **5**, 2659 (2022).

[35] B. Krebs, C. Brendel, and H. Schäfer, Über die reaktion von W_3O mit lod. Darstellung, kristallstruktur und eigenschaften von WOI_3, Z. Anorg. Allg. Chem. **553**, 127 (1987).

[36] M. G. B. Drew and I. B. Tomkins, The crystal and molecular structure of molybdenum(V) oxytribromide, Acta Crystallogr., Sect. B: Struct. Crystallogr. Cryst. Chem. **26**, 1161 (1970).

[37] D. Britnell, G. W. A. Fowles, and D. A. Rice, Adducts of molybdenum(V) trichloride sulphide, J. Chem. Soc., Dalton Trans. (**1975**) 28.

[38] A. A. Vorobyova, E. V. Komleva, M. Y. Geidorf, A. Y. Zaikina, T. M. Vasilchikova, K. V. Zakharov, A. I. Shilov, S. V. Simonov, Y. A. Ovchenkov, I. V. Morozov, L. V. Shvanskaya, S. V. Streltsov, A. N. Vasiliev, and O. S. Volkova, Peculiar crystal structure and long-range order of spin-1/2 ladders in $MoOBr_3$, J. Alloys Compd. **968**, 172072 (2023).

[39] P. Hohenberg and W. Kohn, Inhomogeneous electron gas, Phys. Rev. **136**, B864 (1964).

[40] W. Kohn and L. J. Sham, Self-consistent equations including exchange and correlation effects, Phys. Rev. **140**, A1133 (1965).

[41] G. Kresse and J. Hafner, *Ab initio* molecular dynamics for liquid metals, Phys. Rev. B **47**, 558 (1993).

[42] G. Kresse and J. Furthmüller, Efficiency of *ab-initio* total energy calculations for metals and semiconductors using a plane-wave basis set, Comput. Mater. Sci. **6**, 15 (1996).

[43] A. D. Becke, Density-functional exchange-energy approximation with correct asymptotic behavior, Phys. Rev. A **38**, 3098 (1988).

[44] D. C. Langreth and M. J. Mehl, Beyond the local-density approximation in calculations of ground-state electronic properties, Phys. Rev. B **28**, 1809 (1983).

[45] J. P. Perdew, K. Burke, and M. Ernzerhof, Generalized gradient approximation made simple, Phys. Rev. Lett. **77**, 3865 (1996).

[46] S. Grimme, Semiempirical GGA-type density functional constructed with a long-range dispersion correction, J. Comput. Chem. **27**, 1787 (2006).

[47] S. L. Dudarev, G. A. Botton, S. Y. Savrasov, C. J. Humphreys, and A. P. Sutton, Electron-energy-loss spectra and the structural stability of nickel oxide: An LSDA+U study, Phys. Rev. B **57**, 1505 (1998).

[48] See Supplemental Material at http://link.aps.org/supplemental/10.1103/PhysRevB.110.094408 for the exfoliation energy of vdW bulk WOI_3, phonon spectrum, energies of different FE states of vdW bulk WOI_3, detailed results of projected DOS for 1D WOI_3, the selection of the xy coordinates for PDOS analysis, the influence of U_{eff} on the magnetism of 1D WOI_3, total energies for different magnetic configurations, coefficients of the Heisenberg model, the semischematic phase diagram of 1D WOI_3, brief descriptions and results for the linear response, results of band structures and DOS, additional results for shift current, and which includes Refs. [23,56,66].

[49] R. D. King-Smith and D. Vanderbilt, Theory of polarization of crystalline solids, Phys. Rev. B **47**, 1651 (1993).

[50] X. Wang, R. Wu, D.-s. Wang, and A. J. Freeman, Torque method for the theoretical determination of magnetocrystalline anisotropy, Phys. Rev. B **54**, 61 (1996).

[51] R. Wu and A. J. Freeman, Spin–orbit induced magnetic phenomena in bulk metals and their surfaces and interfaces, J. Magn. Magn. Mater. **200**, 498 (1999).

[52] N. Metropolis, A. W. Rosenbluth, M. N. Rosenbluth, A. H. Teller, and E. Teller, Equation of state calculations by fast computing machines, J. Chem. Phys. **21**, 1087 (1953).

[53] D. Hinzke and U. Nowak, Magnetization switching in a Heisenberg model for small ferromagnetic particles, Phys. Rev. B **58**, 265 (1998).

[54] J. Ibañez-Azpiroz, S. S. Tsirkin, and I. Souza, *Ab initio* calculation of the shift photocurrent by Wannier interpolation, Phys. Rev. B **97**, 245143 (2018).

[55] N. Marzari, A. A. Mostofi, J. R. Yates, I. Souza, and D. Vanderbilt, Maximally localized Wannier functions: Theory and applications, Rev. Mod. Phys. **84**, 1419 (2012).

[56] G. Pizz, V. Vitale, R. Arita, S. Blügel, F. Freimuth, G. Géranton, M. Gibertini, D. Gresch, C. Johnson, T. Koretsune, J. Ibañez-Azpiroz, H. Lee, J.-M. Lihm, D. Marchand, A. Marrazzo, Y. Mokrousov, J. I. Mustafa, Y. Nohara, Y. Nomura, L. Paulatto *et al.*, WANNIER90 as a community code: New features and applications, J. Phys.: Condens. Matter **32**, 165902 (2020).

[57] S. S. Tsirkin, High performance Wannier interpolation of Berry curvature and related quantities with WANNIERBERRI code, npj Comput. Mater. **7**, 33 (2021).

[58] K. Momma and F. Izumi, VESTA 3 for three-dimensional visualization of crystal, volumetric and morphology data, J. Appl. Crystallogr. **44**, 1272 (2011).

[59] A. A. Balandin, F. Kargar, T. T. Salguero, and R. K. Lake, One-dimensional van der Waals quantum materials, Mater. Today **55**, 74 (2022).

[60] Y. Qu, M. Q. Arguilla, Q. Zhang, X. He, and M. Dincă, Ultrathin, high-aspect ratio, and free-standing magnetic nanowires by exfoliation of ferromagnetic quasi-one-dimensional van der Waals lattices, J. Am. Chem. Soc. **143**, 19551 (2021).

[61] G. Mills, H. Jónsson, and G. K. Schenter, Reversible work transition state theory: Application to dissociative adsorption of hydrogen, Surf. Sci. **324**, 305 (1995).

[62] H. Jónsson, G. Mills, and K. W. Jacobsen, Nudged elastic band method for finding minimum energy paths of transitions, in *Classical and Quantum Dynamics in Condensed Phase Simulations*, edited by B. J. Berne, G. Ciccotti, and D. F. Coker (World Scientific, Singapore, 1998), pp. 385–404.

[63] W. Ding, J. Zhu, Z. Wang, Y. Gao, D. Xiao, Y. Gu, Z. Zhang, and W. Zhu, Prediction of intrinsic two-dimensional ferroelectrics in In_2Se_3 and other III_2-VI_3 van der Waals materials, Nat. Commun. **8**, 14956 (2017).

[64] J. L. Lado and J. Fernández-Rossier, On the origin of magnetic anisotropy in two dimensional CrI_3, 2D Mater. **4**, 035002 (2017).

[65] N. D. Mermin and H. Wagner, Absence of ferromagnetism or antiferromagnetism in one- or two-dimensional isotropic Heisenberg models, Phys. Rev. Lett. **17**, 1133 (1966).

[66] Y. Xun, Z. Zhu, X. Chen, and J. Qi, One-dimensional ferromagnetic semiconductor $CrSbSe_3$ with high Curie temperature and large magnetic anisotropy, Phys. Rev. B **104**, 085429 (2021).

[67] S. Dong, H. Xiang, and E. Dagotto, Magnetoelectricity in multiferroics: A theoretical perspective, Natl. Sci. Rev. **6**, 629 (2019).

[68] T. Moriya, New mechanism of anisotropic superexchange interaction, Phys. Rev. Lett. **4**, 228 (1960).